



Cite this: *RSC Adv.*, 2022, **12**, 15316

# Improving the EMI shielding of graphene oxide (GNO)-coated glass-fiber–GNO–MA-grafted polypropylene (PP) composites and nylon 1D–2D nanocomposite foams†

Kanthasamy Raagulan,<sup>a</sup> Jinsoo Ghim,<sup>a</sup> Ramanaskanda Braveenth,<sup>a</sup> Kyu Yun Chai<sup>ID \*a</sup> and Bo Mi Kim<sup>b</sup>

The proliferation of the latest electronic gadgets and wireless communication devices can trigger electromagnetic interference (EMI), which has a detrimental impact on electronic devices and humans. Efficient EMI shielding materials are required for EMI-SE and they should be durable in external environments, lightweight, and cost-effective. GNO-coated glass-fiber–GNO–maleic anhydride-grafted polypropylene (MAPP) composite and carbon fiber-reinforced nylon 1D–2D nanocomposite foam were successfully prepared via a cost-effective thermal process. The composites were characterized using scanning electron microscopy (SEM), Raman spectroscopy, X-ray diffraction (XRD), and X-ray photoelectron spectroscopy (XPS). The PP and nylon-based composites with ~13% filler showed maximum electrical conductivity (EC) of 878 mS cm<sup>-1</sup> and 1381 mS cm<sup>-1</sup>, respectively. The GNO-coated glass-fiber–GNO–MAPP foam displays a maximum EMI-SE of 120.6 dB, while the nylon graphene–carbon nanotube–metal nanoplatelet foam exhibits a maximum EMI-SE of 139.1 dB in the X-band region. The GFCFFeGMAPP composite possesses a minimum thickness of 2.56 mm and blocks most incoming radiation. These are some of the highest EMI-SE values reported so far for glass fiber and nylon-based composites, and the nylon-based composite showed excellent properties compared to the glass fiber-based composite. Thus, we believe that the developed composites can be used in a wide range of real applications, such as in military vehicles, aviation, automobiles, and the packaging of electronic circuits.

Received 17th December 2021  
 Accepted 4th May 2022

DOI: 10.1039/d1ra09124g  
[rsc.li/rsc-advances](http://rsc.li/rsc-advances)

## 1. Introduction

The excessive production of compact electronic devices and upgrading of wireless communication (5G mobile networks) cause inevitable electromagnetic interference (EMI), which is known as electromagnetic pollution in the modern electronic world.<sup>1,2</sup> Long-term exposure to EMI triggers various problems, such as malfunction of adjacent electronic components and health impacts (headache, dizziness, cancer, mutation, and insomnia) on human beings as well as other living organisms. EMI disturbs the natural navigation of migrating birds, which leads to the destruction of ecosystems. In addition, the increasing numbers of digital networks and wireless control systems generate electromagnetic noise (EMN) or destroy

electromagnetic compatibility (EMC).<sup>3</sup> Hence, all electronic devices need EMI shielding systems as the world relies on electronic components.<sup>3–5</sup> Defective EMI shielding causes various issues, such as destruction of security of countries, electronic theft, and destruction of the basic functions of electronic systems. Therefore, achieving EMC in electronic devices is crucial, and EMI shielding is carried out for different regions of electromagnetic radiation (S, C, X, Ku, and microwaves).<sup>1–8</sup>

Total EMI shielding ( $SE_T$ ) is determined by the absorption ( $SE_A$ ), reflection ( $SE_R$ ) multiple reflection ( $SE_{MR}$ ) and transmission ( $T$ ) of electromagnetic radiation hitting shielding materials.  $SE_T$  is calculated by adding  $SE_A$ ,  $SE_R$ , and  $SE_{MR}$ , in which  $SE_{MR}$  is negligible compared to others. Generally,  $SE_A$  influences EMI shielding more than  $SE_R$ , which is generally controlled by the inherent electrical conductivity (EC) of the shielding materials. However, factors such as the dipoles of the materials, structural features, and the thickness of the composite affect the  $SE_A$ . In addition, parameters such as the wave impedance of the air, propagation constant of the wave, relative electric and magnetic permeability, transmission coefficient, angular frequency of the wave, and refractive index also

<sup>a</sup>Division of Bio-Nanochemistry, College of Natural Sciences, Wonkwang University, Iksan City 570-749, Korea. E-mail: [raagulan@live.com](mailto:raagulan@live.com); [pofuin@daum.net](mailto:pofuin@daum.net); [braveenth.czbt@gmail.com](mailto:braveenth.czbt@gmail.com); [geuyoon@wonkwang.ac.kr](mailto:geuyoon@wonkwang.ac.kr); Tel: +82-10-8629-5448

<sup>b</sup>Department of Chemical Engineering, Wonkwang University, Iksan 570-749, Korea. E-mail: [23456@wku.ac.kr](mailto:23456@wku.ac.kr); [123456@wku.ac.kr](mailto:123456@wku.ac.kr); Tel: +82-63-850-7278

† Electronic supplementary information (ESI) available. See <https://doi.org/10.1039/d1ra09124g>



affect the EMI-SE.<sup>7</sup> The MR can be promoted by increasing the thickness of the shielding materials above skin depth, though porous structures also increase the MR, which leads to a good SE<sub>A</sub>. Beyond the shielding ability of the composite, the research community has developed multifunctional materials based on the application domain.<sup>4–8</sup>

EMC is an essential parameter in the modern electronic world and can be accomplished by using various shielding materials, such as zero-dimensional (0D) (quantum dot), one-dimensional (1D) (nanotube and nanowire), two-dimensional (2D) (MXene, and graphene), and three-dimensional (3D) (metals) materials, and various polymers (conductive and nonconductive). Shielding composites are made using one of the above dimensional materials or a combination of materials that are utilized to tune the shielding ability of the composites.<sup>2–5,9,10</sup> Multifunctional shielding materials are developed by mixing diverse type of constitutional components, for which polymers are used as the binder. The binder polymer alters the shielding ability and other parameters of composites. Moreover, conductive polymers (CP) and nonconductive polymers in the composite (CP) significantly enhance properties such as thermal conductivity (TC), tensile strength, electric conductivity (EC), and EMI shielding. In addition, introducing various types of organic and inorganic materials into the matrix can also enhance parameters such as dispersity, adhesivity, porosity, and physiochemical properties of the composites.<sup>5–7</sup> Further, the internal texture (porous, and layered structure), composite preparation method, type of matrix or binder, and type of filler used in the composite greatly influence the EMI shielding and properties of the composites. The porous three-dimensional graphene oxide/polyvinyl alcohol retains an EMI-SE of 43.5 dB with 3.5 mm thickness whereas barium ferrite-decorated graphene oxide exhibits an EMI-SE of 32 dB with thickness of 3 mm (Ku band). However, reduced graphene oxide/silver nanoparticle-decorated conductive cotton fabric exhibits an EMI-SE of 27.36 dB with thickness of 0.29 mm in the X-band region.<sup>8</sup> 3D hierarchical faceted iron oxide-containing vertical carbon nanotubes on a reduced graphene oxide hybrid composite with a thickness of 1 mm exhibits an EMI-SE of 25 dB in the X-band region.<sup>11</sup> Further, ultra-lightweight, water durable and flexible highly electrically conductive polyurethane foam with the thickness of 8.5 mm shows an EMI-SE of 65.6 dB whereas the thermoplastic elastomeric blend (polystyrene/ethylene-co-methyl acrylate copolymer) exhibits an EM-SE of 29.5 dB with thickness of 1 mm.<sup>8,12</sup>

According to Sun *et al.*, a polypropylene (PP)/graphene composite with 0.7 mm thickness showed an EMI-SE of 29.3 dB in the X-band region with EC of  $0.0409 \text{ S cm}^{-1}$ , while MXene/PP composite with filler load of 1.78 vol% displays EMI shielding of 55 dB (1.98 mm thickness and EC of  $4.375 \text{ S cm}^{-1}$ ).<sup>13,14</sup> Further, composites with a 3D conductive network and a porous structure significantly enhance EMI shielding. This is because of the multiple reflection that occurs within the composite, which finally leads to absorption. Lee *et al.* reported that pure PP has no EMI shielding ability but the introduction of 20% conductive fibers into PP with thickness of 2 mm increases the EMI up to 40 dB in the S-band region.<sup>15</sup> Al-

Saleh *et al.* showed that a carbon black (CB)-PP/polystyrene (PS)-styrene–butadiene–styrene (SBS) (95–5–5%) composite with thickness of 2 mm exhibits a maximum EMI-SE of 18.7 dB in the S-band region and the addition of SBS does not affect the EMI-SE of the composite. Further, they stated that EMI-SE is greatly influenced by CB.<sup>16</sup> In addition, the major EMI-SE ability of CB-PP-PS-SBS is due to the SE<sub>R</sub>, as a result of the conductivity created by the introduced fillers.<sup>4</sup> Poothanari *et al.* reported that a polycarbonate (PC)/PP/CNT blend nanocomposite with 2 mm thickness displayed an EMI-SE of 54.78 dB, while immiscible PC/PP composite exhibited an EMI-SE of 22 dB.<sup>17,18</sup> However, a polypropylene/carbon nanotubes composite with 2.8 mm of thickness showed an EMI-SE of 70 dB at 18 GHz frequency, which is relatively higher than that of PC/PP composites.<sup>19</sup> Moreover, the layer-by-layer self-assembly of graphene coating on cotton gave an EMI-SE of 30.04 dB while cotton dip-coated by MWCNTs and cotton knife-over-roll coated with carbon black displayed EMI-SE values of 9 dB and 31.39 dB, respectively.<sup>20</sup> It is obvious that the miscibility of fillers in the matrix, composite preparation techniques, frequency range, filler type, and matrix type significantly influence the EMI-SE. Nevertheless, the shielding materials should possess properties like lightweight, flexible, thin, cost-effective, low density, heat resistance and corrosive resistance. Currently, MXene is an attractive material for EMI shielding applications (92 dB with 45 micron thickness), and has been intensively studied recent years; however, metal plates were conventionally utilized for EMI-SE purposes. According to a recent study, intercalation of different types of nanomaterials in the polymer matrix greatly enhances the EMI-SE and other parameters of composites, like heat resistance, internal structure, and electric conductivity. The EMI-SE is articulated in dB. In addition, weak EMI-SE is below 20 dB while strong EMI is set above 20 dB and can be tuned based on the demand and external stimulation.<sup>3–6</sup>

In this study, we have developed a strategy to achieve higher EMI shielding using different types of composite. We utilized MAPP, graphene oxide-coated glass fiber (GGF) and other fillers as reinforcement components and shielding enhancers. Further, nylon-based composites were prepared without GGF. Non-woven carbon fabrics were used to enhance the EMI-SE and retain the fillers up to some level of the composites. The composite involving glass fiber and the graphene oxide MAPP-based composite is denoted as GFGMAPP (1), whereas the composites with GFGMAPP and non-woven carbon fabric (CF) (2), and non-woven carbon fabric, Fe nanoplatelets, and GFGMAPP (3) are denoted as GFCFGMAPP (2) and GFCFFeGMAPP (3), respectively. For convenience, the composites are denoted using the Arabic numbers 1, 2, and 3. The numbering is used to compare the effect of the thickness of the prepared MAPP-based composites on the shielding behavior. Different types of nylon-based composite were prepared, such as nylon-CF-cobalt nanoplatelet-coated CF-CNT composite (NFCoT), nylon-CF-graphene–CNT composite (NFGT), nylon-graphene–CNT (NGT), and nylon-graphene–copper nanoplatelet composite (NGCu). The composite formulations can be used directly for large-scale industrial production for various structural designs and can facilitate cost-effective designs with less



manpower. The composites showed EMI shielding of over 100 dB in the X-band region, and this study only focused on the EMI shielding ability of composites in the X-band region.

## 2. Materials and methods

### 2.1. Materials

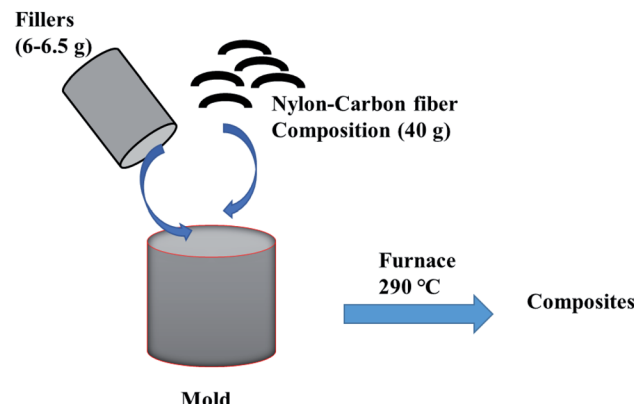
Multiwall carbon nanotubes (MWCNTs) (diameter of 20 nm, CM-90, 90 wt%, and length of 100  $\mu\text{m}$ ) were obtained from Applied Carbon Technology Co. Ltd (Pohang, Korea). Graphene (GN) (M-25, 99.5%, average size of 25  $\mu\text{m}$ , and thickness of 7 nm) was obtained from Ditto Technology Co. Ltd (Gyeonggi-do, Seoul, Korea). Anhydrous cobalt chloride ( $\text{CoCl}_2$ ), anhydrous iron(II) chloride ( $\text{FeCl}_2$  97%), anhydrous copper chloride ( $\text{CuCl}_2$ ), sodium borohydride, sodium dodecyl sulfate (SDS), (3-aminopropyl)triethoxysilane, sulfuric acid ( $\text{H}_2\text{SO}_4$ ), potassium permanganate ( $\text{KMnO}_4$ ), phosphoric acid ( $\text{H}_3\text{PO}_4$ ), hydrogen peroxide ( $\text{H}_2\text{O}_2$ ), graphite, polyacrylamide (PAM), maleic anhydride-grafted polypropylene (MAPP), and cetyltrimethylammonium bromide (CTAB) were bought from Sigma-Aldrich (Seoul, Korea). *N,N*-Dimethylformamide (DMF) was purchased from Daejung (Seoul, Korea), while polyvinylidene fluoride (PVDF) was supplied by Alfa Aesar (Seoul, Korea). Polyethylene terephthalate (PET) binder (fiber diameter 2.2 dtex, 5 mm length) and carbon fiber (fiber diameter 7  $\mu\text{m}$ , 6 mm length) were obtained from TORAY product (Tokyo, Japan). Carbon fiber-reinforced nylon was purchased from T&T Industry (Shenzhen) Co., Ltd (China). Glass fiber (GF) was collected from a local market and cut into small pieces. Ethanol (98%), and hydrochloric acid (HCl 35 wt%), were supplied by Samchun (Seoul, Korea). All the chemicals were utilized as purchased, unless stated.

**2.1.1. Co, Cu, and Fe nanoplatelet synthesis.** Equal amounts ( $1 \text{ g L}^{-1}$ ) of SDS and CTAB were mixed together in deionized (DI) water for 1 h. Then, 0.05 M of  $\text{CoCl}_2$  or  $\text{CuCl}_2$  or  $\text{FeCl}_3$  was added into above solution and stirred for 1 h. Then 0.2 M of cold  $\text{NaBH}_4$  was added dropwise while stirring. The resultant mixture was further stirred for 24 h and washed well with deionized (DI) water. The product was dried in a vacuum oven at 50 °C overnight (Co and Cu nanoplatelets). The products were immediately used for composite preparation.

**2.1.2. Preparation of non-woven carbon fabric (CF) via a wet-laid method.** 150 g of PET binder, 600 g of carbon fiber, and 0.3 wt% of polyacrylamide (PAM) as a dispersant were mixed in an adequate amount of deionized (DI) water at 500 rpm for 10 min. The general wet-laid method is used to create the web, during which the drum dryer surface was kept at 140 °C with a speed of 7  $\text{m min}^{-1}$ . The areal density of the fabric is 30  $\text{g m}^{-2}$ .

**2.1.3. Co-coated carbon fabric.** The Co nanoplatelets and PVDF were mixed at a ratio of 2 : 1 in DMF ( $3 \text{ g L}^{-1}$ ). The resultant mixture was stirred for 24 h and spray-coated on a 15 × 15  $\text{cm}^2$  piece of CF. The drying process was done by using an air gun. The composites were coated 15 times and denoted as CoCF.

**2.1.4. Preparation of various types of nylon composite.** 40 g of carbon fiber-reinforced nylon (CFRN) and 13–14% fillers were



Scheme 1 General nylon-based composite preparation.

filled in a mold and then it was pressed for 5 min. Then the mold was heated at 290 °C in a furnace for 2 h and cooled down to room temperature (RT). The resultant composites were separated, and the thickness of each composite was measured (3–6 mm). The following different kinds of composites were prepared: 40 g of CFRN, 6 g of graphene (GN), and 0.5 g of Cu nanoplatelets used for the nylon-graphene-copper nanoplatelet composite (NGCu) (Scheme S1†), whereas 40 g of CFRN, 3 g of GN, and 3 g of MWCNT were used for the nylon-GN-CNT composite (NGT) (Scheme S2†). The nylon-CF-graphene-CNT composite (NFGT) was prepared by mixing 40 g of CFRN, 3 g of GN, 3 g of MWCNT, and two layers of CF (Scheme S3†) while 40 g of CFRN, 6 g of MWCNT, one layer of Co-coated CF, and two layers of CF were used for the nylon-CF-cobalt nanoplatelet-coated CF-CNT composite (NFCoT) (Scheme S4†) (Scheme 1).

### 2.2. Preparation of maleic anhydride-grafted polypropylene-based composites

**2.2.1. Preparation of surface-modified glass fiber (GF-NH<sub>2</sub>).** 50 g of GF was boiled in DI water for 1 h and then boiled in ethanol for 15 min. Then, the cleaned GF was dried at 150 °C for 1 h. The dried GF was sonicated in 2000 mL of ethanol for 1 h and then added 30 mL of (3-aminopropyl)triethoxysilane, and then, the resultant mixture was heated at 55–65 °C for 3 h. Finally, the silicon-coated GF was washed with a little amount of water and cured at 200 °C for 2 h in a vacuum oven. The final product is denoted as GF-NH<sub>2</sub> (Scheme S5†).

**2.2.2. Graphene oxide (GO) synthesis.** A mixture of 2.25 g of graphite and 300 mL of  $\text{H}_2\text{SO}_4 : \text{H}_3\text{PO}_4$  with 9 : 1 volume ratio was stirred for 5 min. Subsequently, 13.2 g of  $\text{KMnO}_4$  was slowly added into the above mixture and stirred for 6 h. Then, 6.75 mL of  $\text{H}_2\text{O}_2$  was added dropwise into the resultant mixture for 10 min. Finally, 10% HCl was added into the reaction mixture and centrifuged at 5000 rpm for 7 min. The precipitate was washed with HCl/water for 3 times and dried at 90 °C for 24 h. The product is graphene oxide, denoted as GNO.

**2.2.3. Preparation of graphene oxide-coated GF (GGF).** GF-NH<sub>2</sub> was sonicated in water for 1 h, and 16 g  $\text{L}^{-1}$  graphene oxide was added to GF-NH<sub>2</sub>. Then, the resultant mixture was gently stirred for 1 h. Subsequently, black colored fibers were collected



Table 1 Summary of prepared composites

Section	Composition	Abbreviation
2.1.5	Nylon–graphene–copper nanoplatelet composite	NGCu
2.1.6	Nylon–graphene–CNT composite	NGT
2.1.7	Nylon–CF–graphene–CNT composite	NFGT
2.1.8	Nylon–CF–cobalt nanoplatelet-coated CF–CNT composite	NFCoT
2.2.3	Graphene oxide coating on GF–NH <sub>2</sub>	GGF
2.2.4.1	Maleic anhydride-grafted polypropylene graphene oxide mixture	GMAPP
2.2.4.2	GGF–maleic anhydride-grafted polypropylene graphene oxide composite (model 1)	GFGMAPP
2.2.4.3	GGF–CF–maleic anhydride-grafted polypropylene graphene oxide composite (model 2)	GFCFGMAPP
2.2.4.4	GGF–CF–Fe–maleic anhydride-grafted polypropylene graphene oxide nanoplatelet composite (model 3)	GFCFFeGMAPP

using a sieve and dried at 200 °C for 3.5 h in a vacuum oven. Then, the cooled graphene oxide-coated GF–NH<sub>2</sub> was washed with DI water until the water was clear and dried at 200 °C for 1 h. The product is denoted as GGF (Scheme S6†).

**2.2.4. Graphene oxide-coated glass fiber-graphene oxide-maleic anhydride-grafted polypropylene composite preparation.** Maleic anhydride-grafted polypropylene graphene oxide (GMAPP) mixture was prepared by mixing 10 g of maleic anhydride-grafted polypropylene, 2 g of graphene oxide, and xylene together and heating until all the maleic anhydride-grafted polypropylene was dissolved. Then, xylene was evaporated at 100 °C. The resultant maleic anhydride-grafted polypropylene graphene oxide mixture was ground into a powder and denoted as GMAPP. The GGF–GMAPP composite (GFGMAPP) (model 1; Scheme S7†), was made by mixing 30 g of GMAPP and 4.5 g of GGF in the mold and pressing (~50 bar) until it reached 5 mm thickness (Fig. S1†). Then the resultant mold was heated at 180 °C for 2 h and cooled down to RT. This process was repeated for the other composites with different materials. 30 g of GMAPP, 4.5 g of GGF, and one layer of non-woven carbon fabric were used to prepare GGF–CF–GMAPP (GFCFGMAPP) (model 2; Scheme S8†), whereas 0.5 g of Fe nanoplatelets and two layers of non-woven carbon fabric were additionally used to prepare the GGF–CF–Fe–GMAPP nanoplatelet composite (GFCFFeGMAPP) (model 3; Scheme S9 and Fig. S2†). The coating of graphene on functionalized glass fiber is difficult owing to the lack of functional groups on the surface, though graphene oxide can form amide bonds with functionalized glass fiber. Further, maleic anhydride-grafted polypropylene and graphene oxide can form ester bonds at high temperature and mix well due to their polar nature. Thus, graphene-coated glass fibers and GMAPP polymer can form a well intercalated polymer composition (Table 1).

### 2.3. Characterization

The chemical environment and elemental percentage of the composites were measured using XPS with a 30–400 μm spot size at  $E_{\text{max}}$  of 100 W (Al anode) (K-Alpha, Thermo Fisher, East Grinstead, UK). The XRD profiles of the composites were recorded using a high-power X-ray diffractometer (D/max-2500V/PC, Rigaku, Tokyo, Japan) with Cu(K $\alpha$ ). The electrical conductivity (EC) of the composites was measured by using the four-probe method (FPP-RS8, DASOL ENG, Seoul, Korea). A field emission scanning electron microscope (SEM, S-4800, Hitachi,

Tokyo, Japan) was utilized to analyze the surface morphology and cross-section of the composites. A Mitutoyo thickness 2046S dial gauge (Mitutoyo, Kanagawa, Japan) was used to determine the thickness of the composites. High-resolution Raman spectrophotometry (Jobin Yvon, LabRam HR Evolution, Horiba, Tokyo, Japan) was exploited to analyze the structural aspects of the composites. The X-band (8.2–12.4 GHz) EMI shielding was assessed using a vector network analyzer (VNA, Agilent N5230A, Agilent Technologies, Santa Clara, CA, USA) with a sample size of 22.16 mm × 10.16 mm (Fig. S5†).

## 3. Results and discussion

### 3.1. Structural analysis of the composites

**3.1.1. X-ray photoelectron spectroscopy (XPS).** XPS is used to determine the structural nature, surface elemental composition, functionalities, defects, and bonding environment of the compounds. The Gaussian–Lorentzian function of Origin Pro® is exploited to plot the overlapping curves of the composites.<sup>20–22</sup> GFGMAPP gives rise the peaks at 285.14, 532.4, and 102.47 eV, which are responsible for C1s, O1s, and Si2p, respectively, while GFCFGMAPP engenders corresponding elemental peaks at 285.09, 532.1, and 102.52 eV. Further, GFCFFeGMAPP contains elements such as C1s (258.00 eV), O1s (532.18 eV), Si2p (102.24 eV), Fe (2p<sub>1</sub> at 728.26 eV, and 2p<sub>3</sub> at 710.08 eV), whereas GMAPP only consists of C1s (284.93 eV) and O1s (532.47 eV). The C and O are from maleic anhydride-grafted polypropylene (MAPP) graphene oxide and glass fiber whereas Si and Fe are from the glass fiber and Fe nanoplatelets. According to the fitting curve of the PP composites, C1s, O1s, Si2p, and Fe2p are located between 284.37–288.76, 529.8–533.55, 101.93–105.39, and 710.7–734.95 eV, respectively. This indicates that each element maintains various types of bonding in the composites (C–C, C–O, Si–O, Fe–O, O–H) (Fig. S3†). The composite NFCoT comprises elements such as C1s (285.48 eV), N1s (399.95 eV), O1s (531.86 eV), and Co (2p<sub>1</sub> at 799.08 and 2p<sub>3</sub> at 786.69 eV), while C1s (285.53 eV), N1s (400.08 eV) and O1s (803.08 eV) are present in NFGT. The peaks at 285.19, 399.65, and 532.34 eV are due to the C1s, N1s, and O1s of NGF, respectively, although NGCu creates corresponding elemental peaks at 285.22, 400.23, and 532.39 eV, except Cu2p<sub>1</sub> (952.9 eV) and Cu2p<sub>3</sub> (936.79 eV) peaks. C and O are mainly from nylon, GNO, MWCNT, and CF. The N is from nylon and the metals come from the corresponding metal nanoplatelets. According to the fitting curve of the nylon



composites, C1s, N1s, and O1s peaks are situated between 284.59–288.9, 399.1–402.13, and 531.08–533.88 eV, respectively. This indicates that each element hold various types of bonding in the nylon composites (C–C, C–O, N–C, O–H). Hence, the MAPP- and nylon-based composites have different chemical environments (Fig. 1 and S4†).

**3.1.2. X-ray diffraction spectroscopy (XRD) analysis.** XRD is utilized to evaluate the amorphous or crystalline nature of the composites. Sharp peaks represent the crystalline nature of the compound while broad peaks indicate the amorphous nature of the materials. It is apparent that the prepared composites are crystalline in nature (Fig. 2). All the nylon-based composites exhibit sharp  $2\theta$  peaks at 20.2, 24.1, 26.5, 43.4, 54.5, and 79.8°, which confirms that the composites are crystalline in nature. The  $2\theta$  peaks at 20.2° and 24.1° indicate the presence of nylon while 26.5° confirms the occurrence of graphite structure, which is from the carbon fiber in the nylon composite.<sup>21,22</sup> The Bragg angles at 43.4° and 54.5° confirm the occurrence of concentric MWCNT with  $sp^2$  hybridized carbon.<sup>23</sup> In addition, the  $2\theta$  peaks at 25–28° and 54.5° indicate the presence of

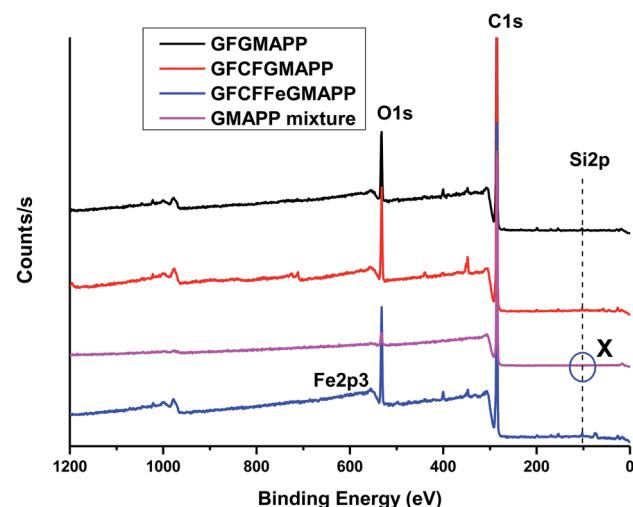
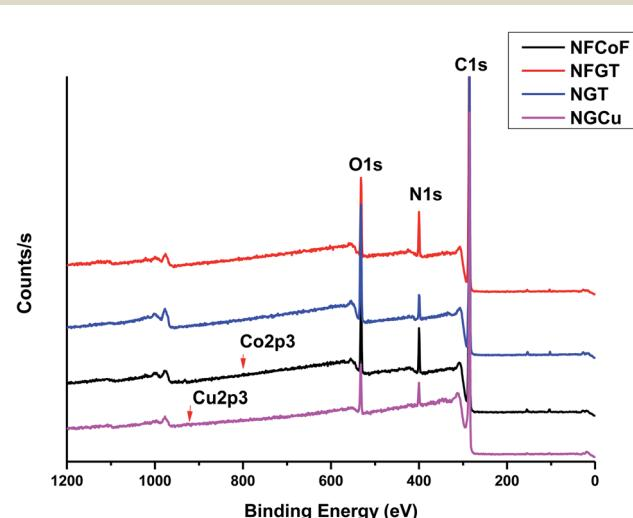


Fig. 1 XPS survey scans of the composites.

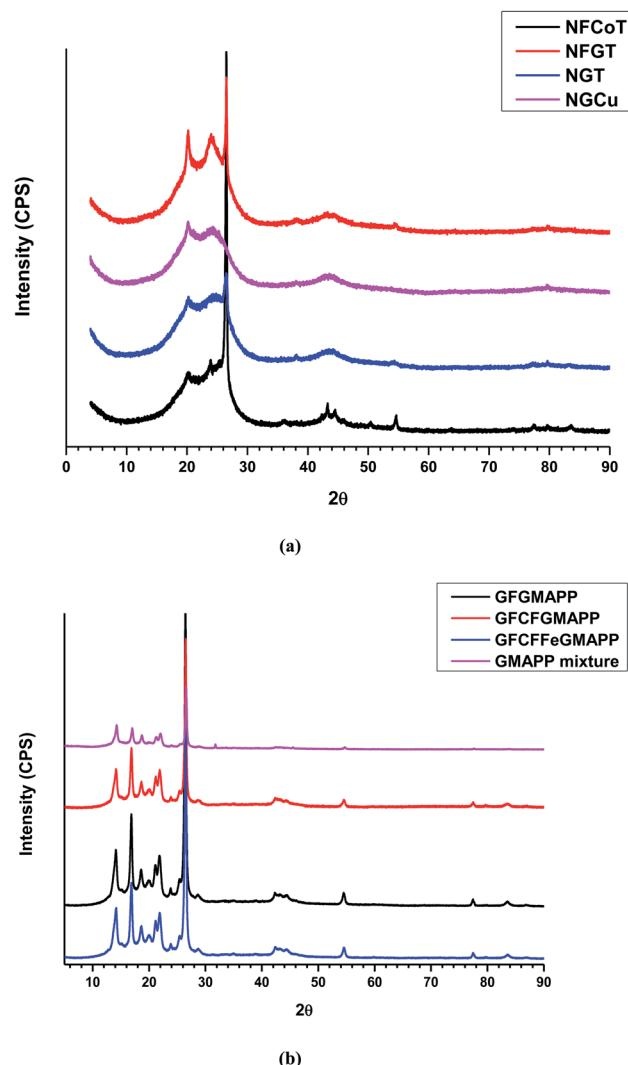


Fig. 2 XRD patterns of the composites.

graphene in the composites.<sup>24</sup> NFCoT shows specific Bragg angles at 35.9, 44.4, 50.5, 77.5, 83.6, and 87.1°, while NFGF exhibits peaks at 38.2, and 44.4°. Among those, 35.9, 44.4 and 77.5° attested the presence of Co nanoplatelets and the shift of the peaks at positions 36.67, 45, and 77.71° affirmed that effective bonding had occurred between the Co nanoplatelets and the composite matrix.<sup>6</sup> NGF displays specific  $2\theta$  peaks at 38 and 83.1° whereas NGCu lost the peak at 26.5°, which is due to the introduction of less Cu nanoplatelets (with no prominent reflection peaks).<sup>24</sup> The broad peaks arise due to the merging of the 20.2 and 24.1° peaks by which nylon composites can be identified. Moreover, this type of pattern is common in the wet-laid carbon fabric used in the nylon composites as the CF source.<sup>8–10</sup> All of the PP composites possess similar sharp Bragg angles at 14.2, 16.8, 18.7, 19.9, 21.3, 21.9, 23.9, 25.5, 26.4, 28.8, 42.4, 43.1, 44.5, 54.5, 77.5, 83.6, and 86.9°, which indicates that all of the PP composites are crystalline in nature. Among these, the  $2\theta$  peaks at 25.5, 26.4, and 54.5° confirm the presence of a graphite-like structure in graphene oxide. Thus, graphene oxide consists of a few layers of graphene sheets together.<sup>24</sup> In



addition,  $2\theta$  peaks between  $14.2$ – $23.9^\circ$  affirm the existence of maleic anhydride-grafted PP.<sup>6,24,25</sup> However, GMAPP shows a peak at  $31.8^\circ$  that disappeared after the composite preparation. This phenomenon shows that effective bonding occurred between PP and other fillers at higher temperature. Further, the GFCFGMAPP shows a specific  $2\theta$  peak at  $79.8^\circ$  by which this composite can be identified. The extra Bragg angles at  $35.2$ , and  $38.8^\circ$  confirm the formation of the GFCFFeGMAPP composites and the presence of Fe nanoplatelets is indicated by the peak at  $38.8^\circ$  in the composites. Hence, the fillers and maleic anhydride-grafted PP interact well and form a strong polymer composition. Both the PP- and nylon-based composites can be used for various applications, including automobiles.

**3.1.3. Scanning electron microscopy (SEM) analysis.** The morphology of the composites is shown in Fig. 3 and 4 in which composites exhibiting aerogel (foam) structure and graphene-coated glass (GGF) fibers are visible. Coral-like structure or aerogel or foam or honeycomb-like structure significantly boost the EMI-SE of the composites. The applied high-pressure compression on the composite creates the compact and layered structure, which increases the intercalation of GGF with the GMAPP polymer composition and reduces the fragility (Fig. S2†). The subsequent heating process produces several bonds with surface graphene oxide and the GMAPP composition. Thus, the composite becomes very hard, therefore, it is difficult to separate from the mold and break into pieces. Hence, the composites were cut into pieces by a cutter, which is obvious in Fig. 3c and f. The presence of maleic anhydride in the GMAPP matrix is responsible for the aerogel structure, which is due to the formation of carbon dioxide. The thermal degradation of the maleic anhydride side chains creates carbon dioxide, which creates many pores, enhancing the fragility of the composites (Fig. 3a–f, and S2†). The lesser amount (1 g) of GGF in the composites creates multiple surface cavities, and the composites are fragile, however, the use of more GGF (4.5 g) in the composites gives higher strength and they are unable to be broken into pieces (Fig. S2†). The presence of unexfoliated graphene oxide gives rise to a layered structure in Fig. 3e, and exfoliated graphene oxide appears as a shrunken sheet between fibers (Fig. 3h). These graphene structures in the composites are beneficial for EMI-SE. The introduction of a small amount of iron nanoplatelets significantly alters the composite structure, where it forms compact aerogel structure similar to that of an ant hill. It is obvious that the lower amount of graphene oxide in the composite alters the composite structure; however, these composites were not used for EMI-SE study due to the fragility (Fig. S2i and j†). Thus, the prepared polypropylene-based composites possess excellent properties with outstanding EMI shielding, which is discussed in Section 3.

The nylon- and polypropylene-based composites are identical and exhibit similar structural features (Fig. 3a–j and 4a–f). The aerogel structure is inherent to the nylon composites. The introduction of metal nanoplatelets and applied pressure narrow down the cavities compared to the unpressed composites (Fig. 4a–d and f). The intercalation of graphene and carbon nanotubes together gives rise to a similar structure of GFCFFeGMAPP, thus, they can be substituted with each other

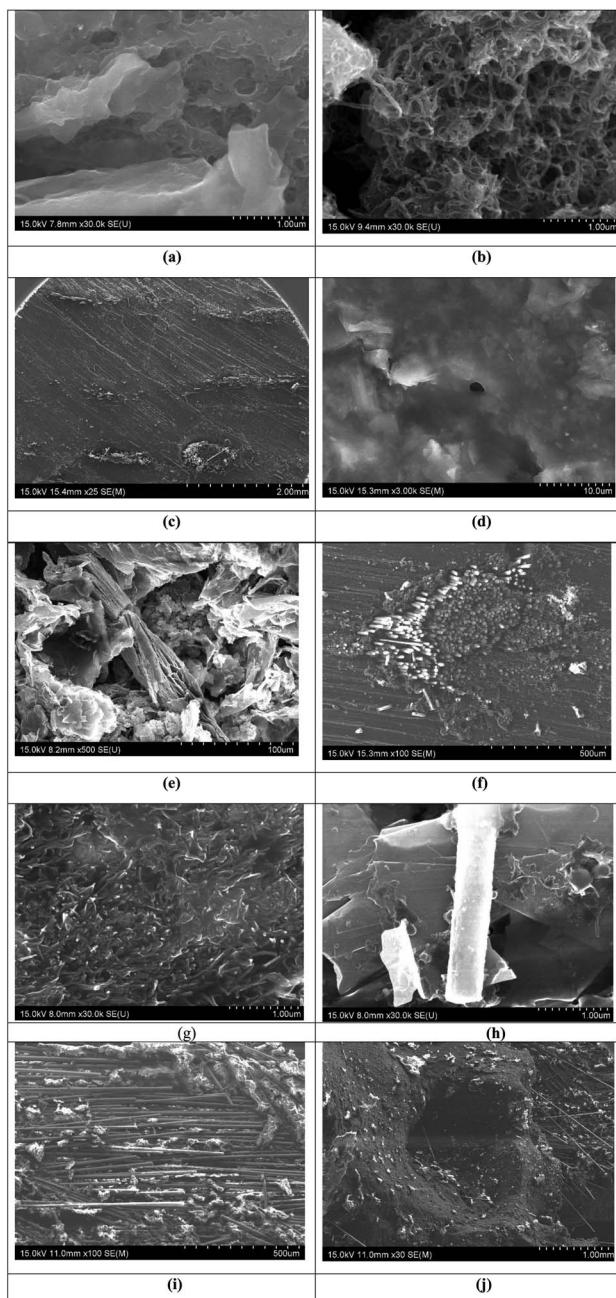


Fig. 3 SEM images of (a) GFGMAPP ( $\times 60$ ), (b) GFCFGMAPP ( $\times 2000$ ), (c) GFCFGMAPP ( $\times 100$ ), (d) GFGMAPP ( $\times 3000$ ) (e and f) GFCFFeGMAPP ( $\times 100$ ), (g) GFCFFeGMAPP, (h) GFCFGMAPP, (i) a composite with 1 g of graphene-coated glass fiber ( $\times 100$ ), and (j) a composite with 1 g of graphene-coated glass fiber ( $\times 30$ ).

as alternatives. The surface of the nylon composite possesses surface cavities with many uneven surfaces and folding, which significantly increases the EMI-SE, but it differs from the polypropylene-based composite (Fig. 3d and 4e). Both the nylon and polypropylene composites give rise to higher EMI-SE compared to the corresponding pure polymers (Fig. 3a–j, and 4a–f). Further explanation is given in Section 3.3.

**3.1.4. Raman spectroscopic analysis of composites.** Raman spectroscopy is a non-destructive and time-resolving tool that is



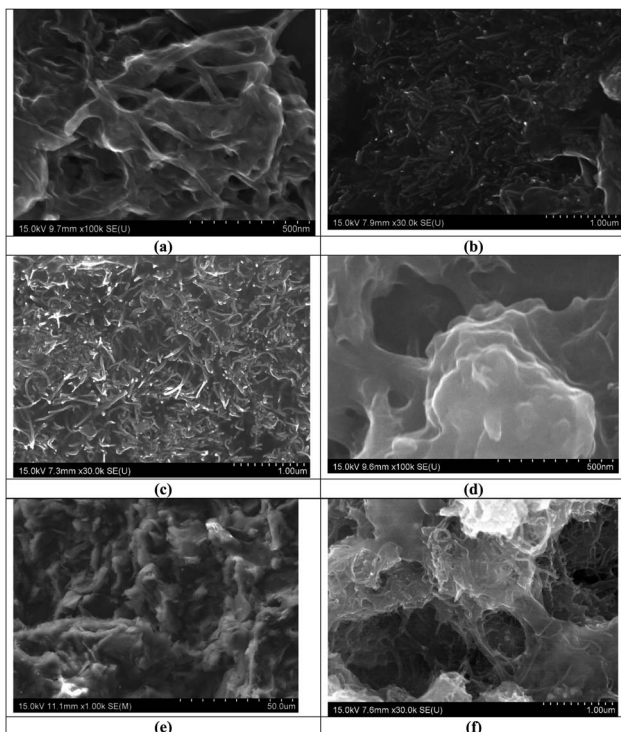


Fig. 4 Surface morphology of (a) NFCoT ( $\times 100\,000$ ), (b) NFGT ( $\times 30\,000$ ), (c) NGT ( $\times 30\,000$ ), and (d) NGCu ( $\times 100\,000$ ). Surface of (e) the nylon composite ( $\times 1000$ ) and (f) the nylon composite without compression ( $\times 30\,000$ ).

utilized to explore the structural features, crystalline nature, level of defects, and physicochemical behaviors of materials, such as graphene, carbon fabric, nanoparticles, CNTs, and composites. The Raman spectra consist of distinctive bands, such as D, G and G' bands. The D band is due to the defects and amorphous nature of the materials, while the graphite structure generates the G band, and an overtone of the D band engenders the G' band. In addition, the level of defects can be explained by using the ratios  $I_D/I_G$  and  $I_D/I_{G'}$ . The increase of both  $I_D/I_G$  and  $I_D/I_{G'}$  values indicates increased of defects. The D band between  $1340\text{--}1350\text{ cm}^{-1}$  is connected with disorder induced by a C-C ring structure, especially  $sp^3$  hybridized carbon, whereas the band between  $1560\text{--}1570\text{ cm}^{-1}$  is due to the stretching of  $sp^2$  hybridized carbon.<sup>23,25</sup> Fig. 5a and b demonstrate the Raman spectra of the composites, which are plotted within  $3500\text{ cm}^{-1}$  Raman shift. GFGMAPP shows peaks at  $320.3, 402.6, 491.3, 601.7, 774.9, 948.1, 1015.2, 1352.8, 1573.6, 2692.6, 2844.2, 2885.3, 2961.1$ , and  $3216.5\text{ cm}^{-1}$ , in which the first four peaks are located at higher intensity compared to the other peaks. GFCFGMAPP gives rise to valleys at  $290.9$  and  $722.1\text{ cm}^{-1}$  and peaks at  $351.5, 396.5, 1355.8, 1466.7, 1582.7, 2718.6, 2839.8, 2890$ , and  $2961\text{ cm}^{-1}$  in which broad downward bands are located between  $351.5$  and  $1355.8\text{ cm}^{-1}$ , while an intense downward band was found at  $290.9\text{ cm}^{-1}$ . GFCFFeGMAPP shows a similar trend up to  $800\text{ cm}^{-1}$  and has various Raman shifts at  $804.5, 848.5, 930.3, 965.2, 1007.6, 1351.5, 1581.8, 2716.7, 2890.9, 2959.1$ , and  $3243.9\text{ cm}^{-1}$ . GMAPP also shows a similar trend like GFCFFeGMAPP up to  $800\text{ cm}^{-1}$ , and

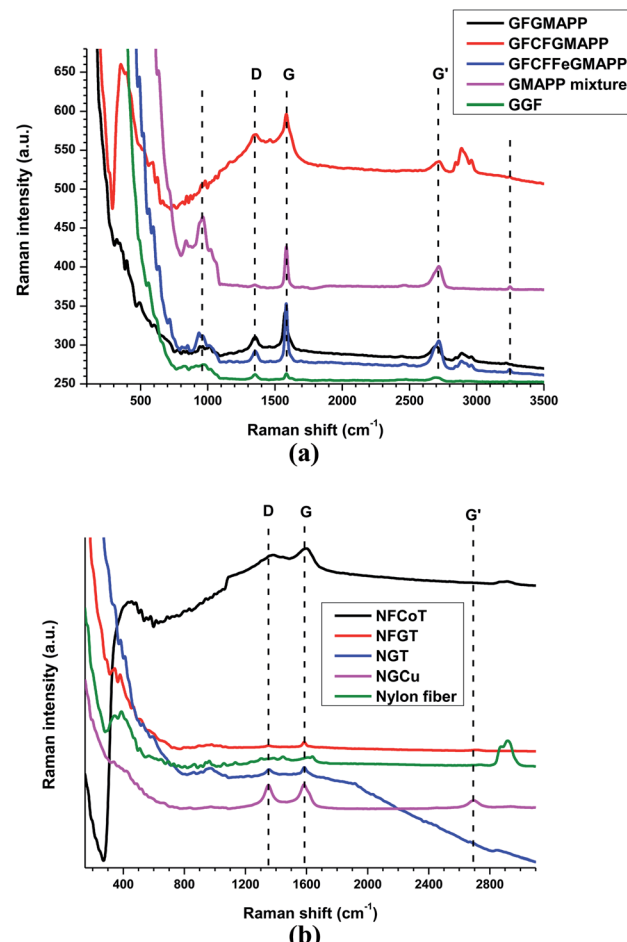


Fig. 5 Raman spectra of (a) PP-based composites and (b) nylon-based composites.

additional Raman shifts are found at  $844.2, 961, 1023.8, 1588.7, 2718.6$ , and  $3244.6\text{ cm}^{-1}$ . Graphene-coated glass fiber (GGF) shows a trend up to  $800\text{ cm}^{-1}$ , which is found in all the polypropylene-based composite and confirms that GGF is responsible for the weak bands found at  $974, 1352.8, 1588.7$ , and  $2699.2\text{ cm}^{-1}$ . NFCoT shows an intense downward band at  $270.6\text{ cm}^{-1}$  and other peaks at  $450.2, 1380.9, 1595.2$ , and  $2913.4\text{ cm}^{-1}$ , whereas NFGT exhibits peaks at  $341.1, 384.4, 467.5, 974.9, 1355.8$ , and  $1587.9\text{ cm}^{-1}$ . NGT displays Raman shifts at  $384.4, 412.1, 964.5, 1350.6, 1582.7$ , and  $1908.2\text{ cm}^{-1}$  whereas NGCu shows Raman shifts at  $335.9, 1350.7, 1582.7, 2696.1, 2945.5$ , and  $3238.1\text{ cm}^{-1}$ , among which  $1350.7$  and  $1582.7\text{ cm}^{-1}$  are shoulder peaks. Nylon fiber shows an intense valley at  $285.7\text{ cm}^{-1}$  and peaks at  $348.3, 387.4, 506.5, 1305.2, 1380.9, 1443.7, 1636.4, 2913.4$ , and  $3305.2\text{ cm}^{-1}$ , among which a broad valley with many miscellaneous peaks occurred between  $506.5\text{ cm}^{-1}$  and  $1305.2\text{ cm}^{-1}$ . The shift in the band position and the disappearance of these peaks in composites confirmed that effective bonding occurred between the nylon fibers and the fillers. The  $I_D/I_G$  ratios for GFGMAPP, GFCFGMAPP, GFCFFeGMAPP, GMAPP, GGF are  $0.62, 0.79, 0.42, 0.48$ , and  $0.93$ , respectively, while the corresponding  $I_D/I_{G'}$  ratios are  $1.31, 1.56, 0.77, 0.66$ , and  $1.32$ . The D bands of the above

composites were located at 1352.81, 1352.81, 1352.81, 1346.32, and 1346.32  $\text{cm}^{-1}$  while the G bands of all the corresponding composites are positioned at 1582.25  $\text{cm}^{-1}$ . Furthermore, G' bands are located at 2692.64, 2712.12, 2718.66, 2718.61, and 2692.64  $\text{cm}^{-1}$ . GGF has the highest level of defects among the composites, however, mixing with polymer and fillers greatly reduced the defects in GGF. There are some parameters that change this phenomenon, namely high temperature, thermal reduction of graphene oxide, GMAPP composition, crosslink with polymer, fillers, and high pressure. The introduction of Fe nanoplatelets diminished the defect of GGF by 55%. The  $I_D/I_G$  value of GMAPP is 0.48, and all other composites have  $I_D/I_G$  values above 0.48, except GFCFFeGMAPP. Thus, introduction of fillers like graphene oxide, CNT, and CF slightly increases the defects. The Fe nanoplatelets not only induce structural perfection but also enhance EMI-SE.<sup>26</sup> The  $I_D/I_G$  ratios of NFCoT, NFGT, NGT, NGCu, and nylon fiber are 0.89, 0.73, 0.99, 0.98, and 1, respectively, while the corresponding  $I_D/I_{G'}$  ratios are 1.1, 1.85, 2.38, 2.65, and 0.55. The D bands of NFCoT, NFGT, NGT, NGCu, and nylon fiber are situated at 1374.46, 1346.32, 1352.81, 1346.32, and 1443.72  $\text{cm}^{-1}$  while the G bands for the corresponding composites are positioned at 1595.24, 1582.25, 1588.74, 1588.74, and 1636.36  $\text{cm}^{-1}$  and the corresponding G' bands are located at 2913.42, 2712.12, 2850.65, 2692.64, 2919.91  $\text{cm}^{-1}$ . It is apparent that pure nylon has more defects than the prepared composites. Therefore, introduction of fillers significantly diminishes the defects.<sup>23,26,27</sup> The porous structure enhances the EMI-SE of all the prepared composites.

### 3.2. Electrical conductivity (EC) of the composites

The EC ( $\sigma$ ) can be calculated from the factors such as resistance ( $R$ ), resistivity ( $\rho$ ), cross-section area ( $A = wt$ , where  $w$  is width and  $t$ , is thickness), length ( $L$ ) and sheet resistance ( $R_s$ ). The EC of the material is reversibly proportional to the  $\rho$  of the material. In addition, the presence of mobile charges in the composites is responsible for their EC and sheet resistance ( $R_s$ ). It is obvious that the composites with the highest  $R_s$  possess lower EC and the  $R_s$  of GFCFGMAPP is beyond the measuring limit (Table 2). The electrical conductivity of graphene is higher than that of graphene oxide, which is true for graphene and graphene-based composites.<sup>24</sup> Many techniques have been developed to boost the EC of composites, such as doping, adding conductive particles (metal particles and carbon-based particles), and incorporation of continuous conductive filaments. Further, the internal structure (segregated structure) of composites with different fillers significantly influences the electrical conductivity of the composites.<sup>24,27-29</sup> The EC range of the composites is 0.407–0.878  $\text{S cm}^{-1}$  while  $R_s$  ranges from 46.39  $\text{ohm sq}^{-1}$  to

Table 3 EC comparison of the nylon-based composites

Sample	Electrical conductivity ( $\text{S cm}^{-1}$ )			
	6 mm	5 mm	4 mm	3 mm
NFCoT	0.361	1.031	0.888	0.964
NFGT	0.260	0.944	0.911	0.867
NGT	0.523	1.015	1.002	1.207
NGCu	1.032	1.381	1.097	1.101

beyond the measurement limit. The variation of the EC of the corresponding composites is due to the unevenly distributed fillers (the thickness of the 6 cm composite is cut to 5, 4, and 3 cm). However, the Fe nanoplatelet-based composite showed excellent EC among the prepared composites. The introduction of fillers such as Fe nanoplatelets and CF significantly enhanced the EC. Furthermore, GFCFGMAPP exhibited a higher EC than that of GFGMAPP (no CF is included). Thus, CF also improves the EC of the composites. The EC of pure PP is in the order of  $10^{-11} \text{ S cm}^{-1}$ , whereas maleic anhydride-grafted PP and fillers significantly improve the EC. The EC of the PP composites depends on polymer grafting, filler amounts, and filler types.<sup>30</sup> The nylon-based composites show EC range of 0.26–1.381  $\text{S cm}^{-1}$  with thickness range of 3–6 mm. It is obvious that the introduction of Cu nanoplatelets significantly enhanced the EC and graphene considerably improved the EC compared to that of CNTs (Table 3). The EC varies based on the thickness, which is due to the filler loading at different level of composite (Fig. S7–S9†). The EC of all of the prepared composites are low, due to which the reflection should be smaller, and EMI-SE is majorly determined by absorption, which is explained more detail in Section 3.3.

### 3.3. EMI shielding abilities of the composites

The EMI-SE shows how well a material quantitatively attenuates the energy of the incoming EMR in a certain frequency range (L, S, C, X, K, Ku, etc. bands). When EMR with specific power ( $P_i$ ) hits the surface of the shielding materials, the EMR undergoes a variety of transformations, such as reflection ( $P_R$ ), absorption ( $P_A$ ), and transmittance ( $P_T$ ).  $SE_R$  occurs on the exterior while  $SE_A$  happens within the shielding materials and the remainder passes on as transmittance EMR.<sup>6</sup>

The  $SE_A$  ( $A$ ) is affected by the nature of the material utilized. The  $A$  and absorption coefficient ( $A_e$ ) can be enunciated as follows, where transmittance ( $T$ ) and reflection ( $R$ ) are interrelated (eqn (1) and (2)).

$$A = 1 - R \quad (1)$$

Table 2 The EC,  $R_s$  and thickness comparison of the PP-based composites

Composite	GFGMAPP (1)	GFCFGMAPP (2)	GFCFFeGMAPP (3)
Electrical conductivity ( $\text{S cm}^{-1}$ )	0.157	0.407	0.878
Thickness (mm)	4.06	4.67	2.56
Sheet resistance ( $\text{ohm sq}^{-1}$ )	46.39	Not measurable	111.60



$$A_e = \left[ \frac{1 - R - T}{1 - R} \right] \quad (2)$$

The mitigation of EMR is defined by shielding effectiveness (SE) and the corresponding unit is dB. The SE can be described as the logarithmic ratio between  $P_i$  and power of transmittance ( $P_t$ ) and can also be explained by using the electric intensity ( $E$ ), magnetic intensity ( $H$ ), wavelength ( $\lambda$ ), and slot length ( $l$ ) of the EMR. The total shielding effectiveness ( $SE_T$ ) is determined by using the following equations, where  $t$  and  $i$  are denoted as transmittance and incident waves, respectively (eqn (3)).

$$SE_T = 10 \log \left( \frac{P_i}{P_t} \right) = 20 \log \left( \frac{H_i}{H_t} \right) = 20 \log \left( \frac{\lambda}{2l} \right) = 20 \log \left( \frac{E_i}{E_t} \right) \quad (3)$$

In addition,  $SE_T$  can be assessed by adding  $SE_A$ ,  $SE_R$ , and  $SE_{MR}$  (eqn (4)).

$$SE_T = SE_R + SE_A + SE_{MR} \quad (4)$$

If the  $SE_T > 15$  dB, the  $SE_{MR}$  is insignificant and the equation can be written as follows (eqn (5)):

$$SE_T = SE_R + SE_A \quad (5)$$

Additionally, the  $T$  and  $R$  can be indicated by using scattering parameters and electric intensity ( $E$ ) in which  $i$  is the incident wave,  $t$  is the transmittance wave, and  $r$  is the reflection wave (eqn (6) and (7)).

$$T = \left| \frac{E_t}{E_i} \right|^2 = |S_{12}|^2 = |S_{21}|^2 \quad (6)$$

$$R = \left| \frac{E_r}{E_i} \right|^2 = |S_{11}|^2 = |S_{22}|^2 \quad (7)$$

Furthermore, the  $SE_T$ ,  $SE_R$ , and  $SE_{MR}$  can be expressed in terms of scattering parameters, wave impedance of air ( $Z_o$ ), wave impedance of the material ( $Z_m$ ), relative magnetic permeability ( $\mu_r$ ), thickness of the shielding materials ( $t$ ), propagation constant ( $\beta$ ), and imaginary unit ( $j$ ) (eqn (8)–(10)).

$$SE_T = 10 \log(T) = SE_R + SE_A = 10 \log \left( \frac{1}{|S_{21}|^2} \right) = 10 \log \left( \frac{1}{1 - |S_{12}|^2} \right) \quad (8)$$

$$SE_R = 10 \log(1 - R) = 20 \log \left| \frac{(Z_o + Z_m)^2}{4Z_o Z_m} \right| \cong 20 \log \left| \frac{Z_o}{4Z_m} \right| = \left( \frac{1}{1 - |S_{11}|^2} \right) \quad (9)$$

$$SE_M = 20 \log \left( \frac{1}{4} \sqrt{\frac{\sigma}{\omega \mu_r \epsilon_0}} \right) = 20 \log |1 - e^{-2t/\delta}| = 20 \log \left| 1 - \left( \frac{Z_o - Z_m}{Z_o + Z_m} \right)^2 e^{-2t/\delta} e^{-2j\beta t} \right| \quad (10)$$

Further, the  $SE_R$ ,  $SE_A$ , and  $SE_{MR}$  can otherwise be delineated by using parameters of the shielding materials, such as refractive index ( $n$ ),  $t$ , skin depth ( $\delta$ ), relative conductivity ( $\delta_r$ ),  $\mu_r$ , and imaginary part of wave vector ( $ik$ ) (eqn (11)–(13)).

$$SE_A = \frac{8.7t}{\delta} = 131.4d \sqrt{f \mu_r \sigma_r} = 10 \log \left[ \frac{T}{(1 - R)} \right] = K \left( \frac{t}{\delta} \right) 10 \log(1 - A_e) = 20 \log e^{t/\delta} = 20 \operatorname{Im}(k) d \log e \quad (11)$$

$$SE_R = 39.5 + 10 \log \left( \frac{\sigma}{2\pi f \mu} \right) 108 + \log \left( \frac{\sigma}{f \mu} \right) = 20 \log \left| \frac{1 + n^2}{4n} \right| \quad (12)$$

$$SE_M = 20 \log \left| 1 - 10^{\frac{SE_A}{10}} \right| = 20 \log \left| \frac{1 - (1 - n^2)}{(1 + n)^2} \exp(2ikd) \right| = 168 + 10 \log \left( \frac{\sigma_r}{\mu f} \right) \quad (13)$$

Skin depth is  $(1/\pi f \delta \mu)$  of the composition where  $f$  is the frequency of the EMR,  $\mu$  is the magnetic permeability, and  $\delta$  is EC (eqn (14)).

$$\delta = \frac{1}{\sqrt{\pi f \sigma \mu}} \quad (14)$$

The propagating EMR changes from near field to far field, which can be explained as  $r < \lambda/2\pi$  is designated as near field and  $r > \lambda/2\pi$  is indicated as far field ( $r$  = distance from EMR source). Hence, most of the EMR is far field and is believed to be planar waves. The impedance of the wave (intrinsic impedance)  $Z$  can be described as the ratio of the amplitudes of the magnetic field ( $H$ ) and electric field ( $E$ ) waves, which are at right angles to each other ( $E \perp H$ ). Moreover, the  $Z$  depends on  $j$ ,  $\mu$ ,  $\delta$ , angular frequency ( $\omega = 2\pi f$ ), and electric permeability ( $\epsilon$ ).  $Z$  of air is designated as  $Z_o$ , and holds a value of  $377 \Omega$  and at this stage  $j$  and  $\omega$  are measured as one and  $\delta$  is zero (eqn (15)–(17)).

$$Z = \frac{|E|}{|H|} \quad (15)$$

$$Z = \sqrt{\frac{j\omega\mu}{\sigma - j\omega\epsilon}} \quad (16)$$

$$Z_o = \sqrt{\frac{\mu_o}{\epsilon_o}} \quad (17)$$

The EMI-SE behavior of the heterogeneous shielding materials (SM) differs from homogeneous SM because



heterogeneous SM consist of more than one material and the physiochemical factors of each component significantly influence the EMI-SE of the composites. The most crucial parameter for the theoretical calculation of the EMI-SE is the effective relative permittivity  $\epsilon_{\text{eff}}$  of the composite, which can be computed by using the Maxwell Garnett formula. The  $\epsilon_{\text{eff}}$  is determined from, the relative permittivity of the matrix ( $\epsilon_e$ ), fillers ( $\epsilon_i$ ), and  $f$ , the volume fraction of the filler. The  $\epsilon_i$  is assessed by using the imaginary part of the complex relative permittivity ( $\epsilon'$  and  $\epsilon''$ ), imaginary unit ( $j$ ),  $\delta$ ,  $\omega$ , and  $\epsilon_0$  (eqn (18) and (19)).

$$\epsilon_{\text{eff}} = \epsilon_e + 3f\epsilon_e \frac{\epsilon_i - \epsilon_e}{\epsilon_i + 2\epsilon_e - f(\epsilon_i - \epsilon_e)} \quad (18)$$

$$\epsilon_i = \epsilon' - j\epsilon'' = \epsilon' - j\frac{\sigma}{\omega\epsilon_0} \quad (19)$$

Besides, the EMI-SE expresses to what extent the composite transmits the EMR, which can be defined by using the transmission coefficient ( $T$ ).  $T$  is dependent on  $T$  at the  $0-t$  boundary ( $T_1$  and  $T_2$ ), the reflection coefficient at the  $0-t$  boundary ( $R_1$  and  $R_2$ ), where 0 is assigned as 1 and  $t$  as 2, and the complex propagation constant ( $\gamma_m$ ). The  $\epsilon$ ,  $j$ ,  $\mu$ , and  $\omega$  alter the  $\gamma_m$  value of the composite (eqn (20) and (21)).

$$T = \frac{T_1 T_2 e^{-\gamma_m D}}{1 + R_1 R_2 e^{-2\gamma_m D}} \quad (20)$$

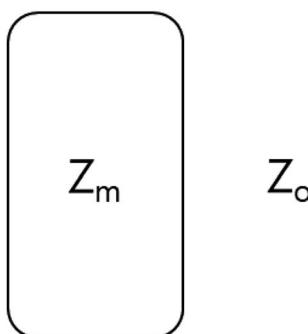
$$\gamma_m = j\omega \sqrt{\epsilon_0 \mu_0 (\epsilon'_{\text{eff}} - j\epsilon''_{\text{eff}})} \quad (21)$$

The  $Z$  of an EMR is the ratio of the transverse components of the magnetic, and electric fields.  $Z_o$  and  $Z_m$  manipulate the magnitude of  $T_1$  and  $R$ . Moreover,  $Z_o$ ,  $\mu_r$ , and  $\epsilon_{\text{eff}}$  influence the value of  $Z_m$  (eqn (22)–(26) and Scheme 2).

$$T_1 = \frac{2Z_m}{Z_m + Z_o} \quad (22)$$

$$T_2 = \frac{2Z_o}{Z_m + Z_o} \quad (23)$$

$$R_1 = \frac{Z_m - Z_o}{Z_m + Z_o} \quad (24)$$



Scheme 2 Indication of  $Z_o$  and  $Z_m$  in a composite.

$$R_2 = \frac{Z_o - Z_m}{Z_m + Z_o} \quad (25)$$

$$Z_m = Z_o \sqrt{\frac{\mu_r}{\epsilon_{\text{eff}}}} \quad (26)$$

Hence, the SE can be described in terms of  $T$ , and the SE of the materials and shielding efficiency in percentage can be calculated based on the  $SE_T$  of the composite (eqn (27) and (28)).<sup>6,7</sup>

$$SE = -20 \log(|T|) \quad (27)$$

$$\text{Shielding efficiency (\%)} = 100 - \left( \frac{1}{10^{SE/10}} \right) \times 100 \quad (28)$$

All the composites prepared in this study show excellent EMI-SE, ranging from 59.99 to 139.1 dB. The maleic anhydride-grafted polypropylene (MAPP)-based composite has EMI-SE maximum (max), average (ave), and minimum (min) ranges of 65.08–120.55 dB, 61.89–102.97 dB, and 59.99–94.53 dB, respectively, with 2.56–11.29 mm thickness (Fig. 6, and Tables S1–S7†). The GFGMAPP (1) with the thickness of 4.06 mm exhibits max, ave, and min EMI-SE of 75.18, 72.76, and 71.72 dB, respectively, whereas GFCFGGMAPP (2) with thickness of 4.67 mm displays 65.08, 61.89, and 59.99 dB, respectively. It is obvious that introduction of CF slightly reduces the EMI-SE with increasing thickness. On the whole, introduction of CF has no impact on the EMI-SE of the composites. However, CF was used to retain the fillers at particular points in the composites. This concept is used in all the composites prepared in this study. Introduction of Fe nanoplatelets in the composite (GFCFFeGMAPP (3)) significantly increases the EMI-SE, giving max, ave, and min EMI-SE of 72.18, 68.94, and 66.29 dB, respectively, with 2.56 mm thickness. Adding composites together during the EMI-SE measurement increases the EMI-SE, as thickness increases, but this process limits the EMI shielding measurement. According to our study of the MAPP-based composites, the threshold average EMI-SE is  $\geq 100$  dB with maximum thickness of 7.23 mm and beyond that the combination of composites (1 + 2 + 3) shows almost similar EMI-SE (Fig. 6, and Tables 3 and S1–S7†). The combination of (2 + 3) engenders max, ave, and min EMI of 120.11, 101.27, and 91.97 dB, respectively, while (1 + 2 + 3) produces max, ave, and min EMI-SE of 120.55, 102.97, and 94.53 dB, respectively. GFGMAPP, GFCFGGMAPP, GFCFFeGMAPP, (2 + 3), and (1 + 2 + 3) have maximum  $SE_A$  of 69.97, 62.19, 67.39, 113.36, and 113.52 dB, respectively, whereas the corresponding  $SE_R$  are 6.68, 4.79, 5.73, 7.38, and 7.40 dB (Fig. 6 and Tables S1–S4 and S7†). The  $SE_A$  of the prepared composites are higher than the  $SE_R$ , thus,  $SE_A$  is more dominant than  $SE_R$ . According to our study, the pure PP/GGF composite possesses EMI shielding of about 1 dB, which cannot be used for industrial application (Fig. S6†). Thus, we modified the structure of the composites and got the highest EMI shielding values for various thickness (Fig. 6, and Tables S1–S7†). The polypropylene/carbon nanotubes composite shows



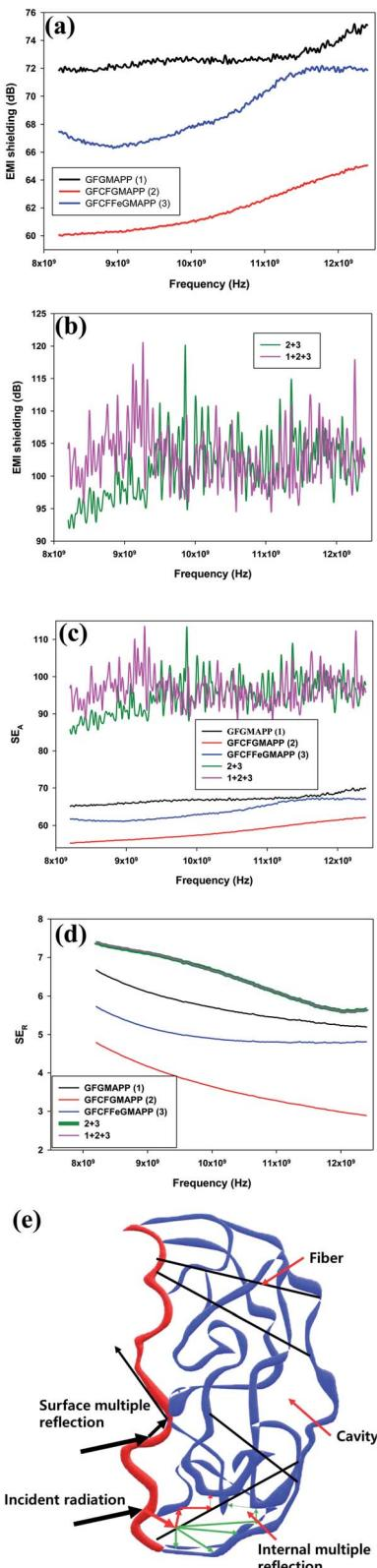


Fig. 6 EMI shielding of PP composites: (a)  $SE_T$ , (b)  $SE_T$  of multilayer compositions, (c)  $SE_A$ , and (d)  $SE_R$ . (e) The EMI-SE mechanism of all composites.

EMI-SE of 70 dB with 2.8 mm thickness at 18 GHz frequency, which is lower than that of GFCFFeGMAPP in X-band.<sup>19</sup> Therefore, the prepared composite possesses excellent shielding ability compared to the PP/CNT composite. This study primarily focused on the miscibility of fillers in the matrix, by which the EMI-SE was enhanced greatly (Section 2). In addition, when preparing the PP-based composites, the fillers are mixed with dissolved PP in xylene and then the solvent is evaporated. Thus, the prepared composites showed excellent EMI shielding for various EMI shielding applications.

The nylon-based composites show excellent EMI shielding of >100 dB with 4 mm thickness. The maximum EMI shielding range of the composites is situated between 139.1–61.4 dB in the thickness range of 6–3 mm, whereas the corresponding  $SE_A$  and  $SE_R$  ranges are 131.6–60 dB, and 9.9–7.9 dB, respectively. It is obvious that the  $SE_T$  is determined by the  $SE_A$  than the  $SE_R$ , which is due to the foam structure developed in the nylon-based composites. The max EMI-SE of NFCoT, NFGT, NGT, and NGCu are 132.9, 139.1, 129.4, and 138.8 dB, respectively, while the corresponding ave EMI-SE are 108.4, 108.9, 108.7, and 108.2 dB, respectively. The max  $SE_A$  of NFCoT, NFGT, NGT, and NGCu are 123.5, 130.8, 122.5, and 131.6 dB, respectively, while the corresponding ave  $SE_A$  are 99.9, 99.4, 101.9, and 100.5 dB, respectively. The max  $SE_R$  of NFCoT, NFGT, NGT, and NGCu are 9.7, 9.4, 7.9, and 9.9 dB, respectively, whereas the corresponding ave  $SE_R$  are 8.4, 8.3, 6.8, and 7.7 dB, respectively. According to our observation, reducing the thickness by cutting increases the EMI-SE significantly, which is due to the exposure of the internal porous structure. When the internal porous structure is exposed to the incident radiation, the incident radiation undergoes surface reflection, MR and  $SE_A$ . This phenomenon is obvious in NFGT where  $SE_T$  with 6 mm and 5 mm are 132.4, and 139.1, respectively, and corresponding  $SE_A$  are 124.8, and 130.8 dB. However, the  $SE_R$  are similar; at 9.7 and 9.4 dB, respectively. According to the nylon-based composite, the graphene, CNT, and Cu nanoplatelet fillers are better than the Co nanoplatelet filler for higher EMI with less thickness. The layer-by-layer self-assembly of graphene-coated cotton shows EMI-SE of 30.04 dB while dipped coated cotton by MWCNT exhibits EMI-SE of 9.0 dB. Furthermore, cotton knife-over-roll coated with carbon black displays an EMI-SE of 31.39 dB.<sup>30</sup> It is obvious that the composite preparation technique and type of fillers influence the EMI-SE. Therefore, this study also proved that gradual filling of the composite into the mold with multiple pressing greatly increase the EMI compared to single pressing of the composite (Fig. 7a–d, S7–S9, S10–S12a–d†). The multiple pressing of the composite increased the EMI-SE greatly (139.1 dB), though single pressing gave rise to an average of 60 dB. Thus, this process increases EMI-SE by 2.3 times. The composites were prepared without any solvent, thus, we described it as a solid phase process. Therefore, this is mostly suitable for industrial scaleup. This is a cost-effective process as there is no solvent used and no need for extra skill to prepare the composites. The thermoplastic polyurethane (TPU)-reinforced CF with 0.66 mm thickness shows EMI-SE of 19.4 dB, whereas double and triple layer show EMI-SE of 45.5 and 80.5 dB, respectively. The EMI-SE of multiple layer fabrics depends on the stacking angle of the

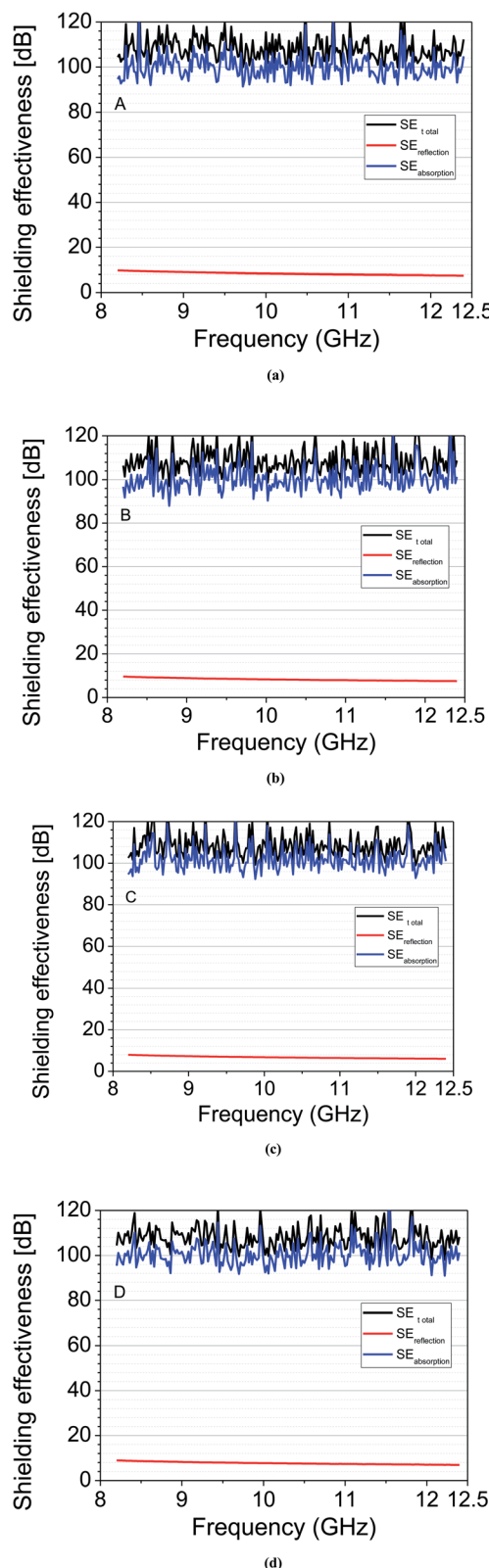


Fig. 7 EMI-SE of composites with a thickness of 6 mm: (a) NFCoT, (b) NFGT, (c) NGT, and (d) NGCu.

fabric, though there is less effect with thinner fabric. The MWCNT/TPU with 2 mm thickness engenders an EMI-SE of 22 dB.<sup>31</sup> The comparison of the different composites is tabulated in

Table S7.<sup>†</sup> As the composites possess a porous structure with surface cavities, the EMI-SE mechanism can be explained as follow; the incident electromagnetic radiation (EMR) hits on the surface of the shielding material; a particular amount of radiation penetrates, while the remaining undergoes reflection and surface absorption. The penetrated EMR experiences multiple reflection, which finally leads to absorption. When the thickness of the composite increases, the probability of multiple reflection (MR) increase significantly, thus,  $SE_A$  is higher at higher thickness. Further, GGF and CF also partake in MR. However, MR is dependent on the types of fillers used (Fig. 6e). The composites were especially prepared for automobile applications, and a schematic illustration of an EMI-SE cover (of an electric circuit) is shown in Fig. S18<sup>†</sup> with the upper, lower, and side views of the cover. Similar designs can be used for other applications, such as military vehicles, aviation, other automobile spare parts, and electronics (Fig. S18<sup>†</sup>).

## 4. Conclusions

Graphene oxide-coated GF-GMMAP and CFRN-graphene-carbon nanotube–metal nanoplatelet composites were successfully prepared *via* a heat-based process. The prepared GGF-GMAPP composite thickness varied between 2.56 and 4.67 mm, whereas the thickness of the CFRN-based composites ranged from 3 to 6 mm. The  $SE_A$  and  $SE_R$  ranges of the MAPP-based composites are 113.52–55.22 dB and 7.40–2.88 dB, respectively, and the  $SE_T$  range of the composites lies between 59.99 and 120.55 dB. The EMI-SE range of the nylon-based composites was 61.4–139.1 dB, and the NFGT-based composites revealed the highest EMI-SE of 139.1 dB with a thickness of 5 mm. The  $SE_A$  and  $SE_R$  ranges of the nylon-based composites are 131.6–53.5 dB and 6.1–9.9 dB, respectively. Thus,  $SE_A$  is a more dominant EMI shielding parameter than  $SE_R$ , and it is about 14 times higher than  $SE_R$ . The MAPP-based composites showed an EC range of 878–157 mS cm<sup>-1</sup>, whereas the nylon-based composites exhibited an EC range of 260–1381 mS cm<sup>-1</sup>. Our study found that the nylon-based composites exhibited better overall performance compared to the MAPP composites. This study shows a path towards the development of highly efficient EMI shielding materials for various practical applications.

## Funding

This research received no external funding.

## Author contributions

K. Y. C. supervised the project; K. R., and R. B. designed the project; B. M. K. supervised the lab; K. R., B. M. K., and J. S. G. performed the experiments; K. R., and J. S. G. analyzed the data; R. B. supervised the analysis and writing; K. R. and J. S. G. wrote the manuscript.

## Conflicts of interest

The authors declare no conflicts of interest.



## Acknowledgements

This work was supported by Wonkwang University in the year of 2021.

## References

- 1 P. Song, B. Liu, C. Liang, K. Ruan, H. Qiu, Z. Ma, Y. Guo and J. Gu, *Nano-Micro Lett.*, 2021, **13**, 1–7.
- 2 X. Jia, B. Shen, L. Zhang and W. Zheng, *Chem. Eng. J.*, 2021, **405**, 126927.
- 3 Y. Liu, Q. Wu, L. Liu, P. Manasa, L. Kang and F. Ran, *J. Mater. Chem. A*, 2020, **8**, 8218–8233.
- 4 C. Liang, H. Qiu, P. Song, X. Shi, J. Kong and J. Gu, *Sci. Bull.*, 2020, **65**, 616–622.
- 5 B. Yao, W. Hong, T. Chen, Z. Han, X. Xu, R. Hu, J. Hao, C. Li, H. Li, S. E. Perini and M. T. Lanagan, *Adv. Mater.*, 2020, **32**, 1907499.
- 6 K. Raagulan, J. S. Ghim, R. Braventh, M. J. Jung, S. B. Lee, K. Y. Chai, B. M. Kim and J. Lee, *Nanomaterials*, 2020, **10**, 2086.
- 7 K. Raagulan, B. M. Kim and K. Y. Chai, *Nanomaterials*, 2020, **10**, 702.
- 8 S. Ghosh, S. Ganguly, S. Remanan, S. Mondal, S. Jana, P. K. Maji, N. Singha and N. C. Das, *J. Mater. Sci.: Mater. Electron.*, 2018, **29**, 10177–10189.
- 9 R. K. Singh, R. Kumar and D. P. Singh, *RSC Adv.*, 2016, **6**, 64993–65011.
- 10 R. Kumar, R. K. Singh, P. K. Dubey, P. Kumar, R. S. Tiwari and I. K. Oh, *J. Nanopart. Res.*, 2013, **15**, 1–10.
- 11 R. Kumar, A. V. Alaferdov, R. K. Singh, A. K. Singh, J. Shah, R. K. Kotnala, K. Singh, Y. Suda and S. A. Moshkalev, *Composites, Part B*, 2019, **168**, 66–76.
- 12 S. K. Ghosh, T. K. Das, S. Ghosh, S. Remanan, K. Nath, P. Das and N. C. Das, *Compos. Sci. Technol.*, 2021, **210**, 108800.
- 13 T. Sun, W. Luo, W. Luo, Y. Wang, S. Zhou, M. Liang, Y. Chen and H. Zou, *Ind. Eng. Chem. Res.*, 2020, **59**, 11206–11218.
- 14 M. K. Xu, J. Liu, H. B. Zhang, Y. Zhang, X. Wu, Z. Deng and Z. Z. Yu, *Ind. Eng. Chem. Res.*, 2021, **60**, 4342–4350.
- 15 P. C. Lee, B. R. Kim, S. K. Jeoung and Y. K. Kim, *AIP Conf. Proc.*, 2016, **1713**, 120015.
- 16 M. H. Al-Saleh and U. Sundararaj, *Macromol. Mater. Eng.*, 2008, **293**, 621–630.
- 17 A. Kaushal and V. Singh, *Polym. Compos.*, 2021, **42**, 1148–1154.
- 18 M. A. Poothanari, J. Abraham, N. Kalarikkal and S. Thomas, *Ind. Eng. Chem. Res.*, 2018, **57**, 4287–4297.
- 19 H. Lecocq, N. Garois, O. Lhost, P. F. Girard, P. Cassagnau and A. Serghei, *Composites, Part B*, 2020, **189**, 107866.
- 20 M. Tian, M. Du, L. Qu, S. Chen, S. Zhu and G. Han, *RSC Adv.*, 2017, **7**, 42641–42652.
- 21 A. M. Leite, L. F. Maia, E. M. Araujo and H. L. Lira, *J. Appl. Polym. Sci.*, 2009, **113**, 1488–1493.
- 22 K. Raagulan, R. Braventh, H. J. Jang, Y. S. Lee, C. M. Yang, B. M. Kim, J. J. Moon and K. Y. Chai, *Bull. Korean Chem. Soc.*, 2018, **39**, 1412–1419.
- 23 K. Raagulan, R. Braventh, L. R. Lee, J. Lee, B. M. Kim, J. J. Moon, S. B. Lee and K. Y. Chai, *Nanomaterials*, 2019, **9**, 519.
- 24 K. Raagulan, R. Braventh, H. J. Jang, L. Y. Seon, C. M. Yang, B. M. Kim, J. J. Moon and K. Y. Chai, *Materials*, 2018, **11**, 1803.
- 25 T. N. Moja, N. Bunekar, S. B. Mishra, T. Y. Tsai, S. S. Hwang and A. K. Mishra, *Sci. Rep.*, 2020, **10**, 1–4.
- 26 F. López-Barajas, L. F. Ramos-DeValle, S. Sánchez-Valdés, E. Ramírez-Vargas, G. Martínez-Colunga, A. B. Espinoza-Martínez, S. Flores-Gallardo, J. Mendez-Nonell, A. B. Morales-Cepeda, T. Lozano-Ramirez and F. I. Beltrán-Ramírez, *Polym. Test.*, 2019, **73**, 346–351.
- 27 X. Li, P. Bandyopadhyay, T. T. Nguyen, O. K. Park and J. H. Lee, *J. Membr. Sci.*, 2018, **547**, 80–92.
- 28 S. Abbasi, R. B. Ladani, C. H. Wang and A. P. Mouritz, *Mater. Des.*, 2020, **195**, 109014.
- 29 S. H. Park, J. Hwang, G. S. Park, J. H. Ha, M. Zhang, D. Kim, D. J. Yun, S. Lee and S. H. Lee, *Nat. Commun.*, 2019, **10**, 1.
- 30 M. Nisar, C. P. Bergmann, J. Geshev, R. Quijada and G. B. Galland, *Polymer*, 2017, **118**, 68–74.
- 31 N. Duan, Z. Shi, J. Wang, G. Wang and X. Zhang, *Macromol. Mater. Eng.*, 2020, **305**, 1900829.

